Editors' Suggestion

Laboratory modeling of moist convection using a reactive fluid

Valentin Dorel [*]
CNRS, Aix Marseille Université, Centrale Marseille, IRPHE, Marseille, France

Daniel Lecoanet [†]
Department of Engineering Sciences and Applied Mathematics and Center for Interdisciplinary Exploration and Research in Astrophysics, Northwestern University, Evanston, Illinois, USA

Michael Le Bars [‡]
CNRS, Aix Marseille Université, Centrale Marseille, IRPHE, Marseille, France

(Received 27 January 2025; accepted 23 April 2025; published 23 May 2025)

We present a laboratory experiment to model convection in the atmosphere driven by latent heat of condensation ("moist convection"). The system consists of a tank filled with an aqueous solution containing a color indicator that renders the fluid yellow and transparent when acidic and blue and opaque when basic. A sodium lamp positioned above the tank serves as a heat source. Initially, the solution is entirely acidic and stably stratified in temperature. A basic layer is progressively generated at the tank's bottom through water electrolysis, forming an initially stable, blue region. This layer is internally heated by absorbing the heat from the sodium lamp, modeling the latent heat of condensation in the atmosphere. Over time, instabilities develop at the interface between the yellow and blue layers. We investigate the variation of the instability wavelength and complement our observations with a linear stability analysis to elucidate the underlying mechanisms and the process of wavelength selection. Direct numerical simulations are then employed to explore the first steps of the nonlinear regime in connection with experimental observations.

DOI: 10.1103/PhysRevFluids.10.053505

I. INTRODUCTION

Convection refers to fluid motion driven by buoyancy differences and is a fundamental process in geophysical settings. One of the most studied cases is Rayleigh-Bénard convection, where a fluid layer is heated from below and cooled from the top. When the temperature contrast between the two plates is sufficiently large the system becomes unstable and convection results. Most research focuses on how turbulent convection transports heat and momentum through the layer (see [1] for a review). Another well-studied phenomenon is double-diffusive convection, in which two agents (typically temperature and salinity) influence buoyancy. If these agents have different diffusion coefficients, instabilities can arise even when the fluid's density increases downward. The convection pattern depends strongly on whether the destabilizing agent has a higher or lower diffusivity (see [2] for details). While double-diffusive convection is commonly associated with

[*]Contact author: valentin.dorel@univ-amu.fr
[†]Contact author: daniel.lecoanet@northwestern.edu
[‡]Contact author: michael.le-bars@univ-amu.fr

oceanography [3,4], it is also believed to play a role in the evolution of massive stars and giant planets [5], as well as influencing the dynamics of magma chambers [6] and Earth's crust [7].

Convection in the Earth's atmosphere, however, is quite different from the idealized case of Rayleigh-Bénard convection. The main feature of atmospheric convection is the presence of water vapor which, when it condenses, releases latent heat. The latent heat release is a source of internal heating quite distinct from the boundary heating often studied, e.g., in Rayleigh-Bénard convection [8]. Condensation occurs when the humidity of an air parcel is larger than the saturation humidity, which is itself a function of temperature. The saturation humidity generally decreases with height, leading to internal heating for rising saturated air parcels. But at the same time, rising air parcels also mix with the ambient air, decreasing their mean humidity, potentially causing the parcel to become unsaturated. A dry stable state can become unstable in the presence of moisture, depending on the balance between those two effects [9].

A better understanding of moist convection is key in climate modeling, and clouds remain one of the main sources of uncertainty in predicting the future climate change because of the complex multiscale physics involved [10]. Mixing at the top of clouds involves many processes such as evaporative cooling and radiative cooling, and numerous models, simulations, and experiments have been developed to study this mixing (see [11] for a review). Numerical atmospheric models often rely on subgrid parametrization [12]. Some typical behaviors of moist convection, such as cloud aggregation, have been studied numerically [13], but a fundamental understanding of the mechanisms determining typical length scales, velocities, and heat fluxes—similar to what is known for Rayleigh-Bénard convection [14]—remains lacking.

Recently, Vallis *et al.* [15] developed a simplified mathematical model of moist convection to bridge the gap between Rayleigh-Bénard and atmospheric convection. This model incorporates an active condensate into the Rayleigh-Bénard equations, accounting for the effects of internal heating above a threshold within an initially stable background stratification. It captures the interplay between both internal heating and mixing of ambient dry air, in a rising saturated air parcel. Notably, it does not include the liquid phase, thereby neglecting the dynamics of raindrops for simplicity. Experimental analogs of moist convection have also been developed in the past years, reproducing, for example, the internal heating with Ohmic heating [16] or using phase change [17].

In this work we aim to develop an analog of moist convection and of the "Rainy-Bénard" model of Vallis *et al.* [15] in a laboratory experiment (see further discussion in Appendix). Our setup is inspired by the experiments of Sayler and Breidenthal [18], who explored radiative entrainment at the top of stratiform clouds, and Krishnamurti [19], who investigated conditional instability. The present paper focuses on presenting the experimental setup, together with theoretical modeling and numerical simulations, while addressing the challenges encountered in each approach. We also discuss the onset of instability. In Sec. II we describe the experimental setup and typical behaviors. We focus on the observed instability and how its wavelength varies with the control parameters. In Sec. III we derive a full nonlinear model describing the experiment, which is then linearized. We also propose a simple model for the instability mechanism, demonstrating how it differs from classical convective instabilities while resembling that of moist convection. A linear stability analysis, using a quasistatic approach, is presented in Sec. IV. We compare the linear stability results with the experimental data and qualitatively interpret the growth rate evolution and the wave number selection. Finally, in Sec. V we describe the early stages of nonlinear evolution using direct numerical simulations, focusing on the merging of plumes.

II. EXPERIMENTAL SETUP AND RESULTS

Our experimental setup is inspired by Krishnamurti [19] and is sketched in Fig. 1. We use a rectangular tank of dimensions $32\,\mathrm{cm} \times 32\,\mathrm{cm} \times 20\,\mathrm{cm}$ (we define $H = 20\,\mathrm{cm}$ to be the height of the tank), filled with an homogeneous solution of distilled water, sulfuric acid, and bromothymol blue (BTB), a color indicator. The concentration of sulfuric acid is chosen to have an initial $\mathrm{pH}_i = 5$. We define c_T to be the concentration of BTB. A BTB solution is yellow and transparent at $\mathrm{pH} < 7$

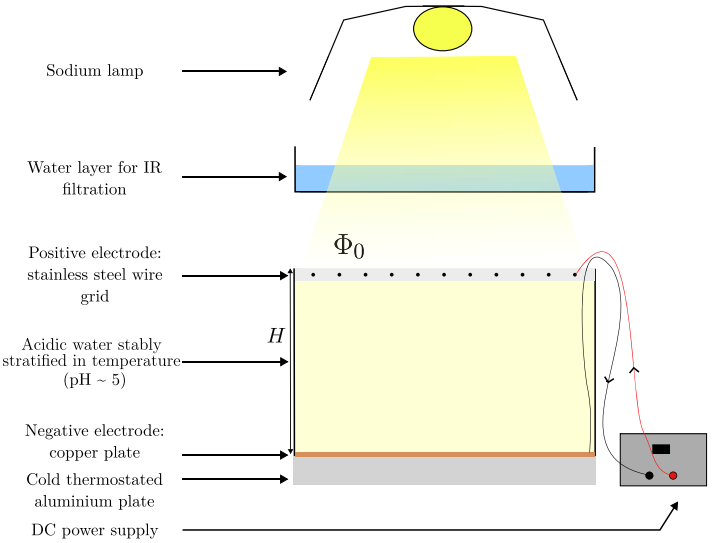

FIG. 1. Sketch of the experimental setup.

and blue and opaque at higher pH. A dc power supply applies a constant voltage U between a stainless steel wire grid placed at the top of the tank and a copper plate placed at the bottom of the tank. This voltage induces the water electrolysis: at the top electrode, water is consumed to produce O_2 and H^+; at the bottom electrode, water is consumed to produce H_2 and HO^-. The solution close to the top electrode becomes more acidic and the solution close to the bottom one becomes more basic, and hence blue. Below the negative electrode, an aluminum plate connected to a thermostated bath fixes the temperature. The electrolysis current I is measured with a clamp meter. A 1-kW sodium lamp (HPS 1000 W ET25) is placed at the top of the experimental setup. A layer of water is placed between the lamp and the working tank to filtrate the IR radiations so that the yellow fluid will not be heated by the light flux. We define Φ_0 to be the irradiance (in $\mathrm{W/m^2}$) at the top of the tank. A uEye Cockpit camera is used to record the flow from the side at a frame rate $f = 0.5\,\mathrm{Hz}$, as all the motions are very slow in our experiment.

Before the start of the experiment, the aqueous solution is stably stratified in temperature with a temperature contrast ΔT between the top and the bottom. Then the lamp and power supply are turned on. Electrolysis creates a bottom blue layer that grows by diffusion. This blue layer absorbs the radiations of the light and heats internally. The threshold for heating is here in terms of pH: for $\mathrm{pH} < 7$, the solution is yellow and does not heat, while for $\mathrm{pH} > 7$, the solution is blue, absorbs the light, and heats. An instability develops at the interface between the two layers and plumes of blue fluid rise in the ambient yellow (Fig. 2). The observed rise of the plumes is always very slow ($v_{\mathrm{rise}} \leqslant 50\,\mu\mathrm{m\,s^{-1}}$). As water electrolysis creates H_2 at the bottom electrode, if the electrolysis current I is too large, rising H_2 bubbles will entrain the ambient fluid. To avoid this effect, we reduced the current until the bubble perturbations disappeared: either the bubbles are too small to entrain a significant part of the blue fluid or they dissolve in the ambient. In the end we worked with $I \leqslant 3\,\mathrm{mA}$, for which no entrainment effect was observed. While others have found chemical instabilities at the interface due to the small difference in buoyancy between the reactants and products [20], those instabilities were only observed for much higher acid/base concentrations than used here, and we did not see any evidence of such instabilities in the experiments presented in this article.

Let us now describe some qualitative experimental observations and measurements. The easiest parameter to vary in our experiment is the concentration of BTB, c_{T}. Defining ε to be the peak value of the molar extinction coefficient of the blue form of BTB, $\delta = 1/\varepsilon c_{\mathrm{T}}$ is the typical length scale over which light is absorbed in the blue layer. A high concentration of BTB results in a high heating

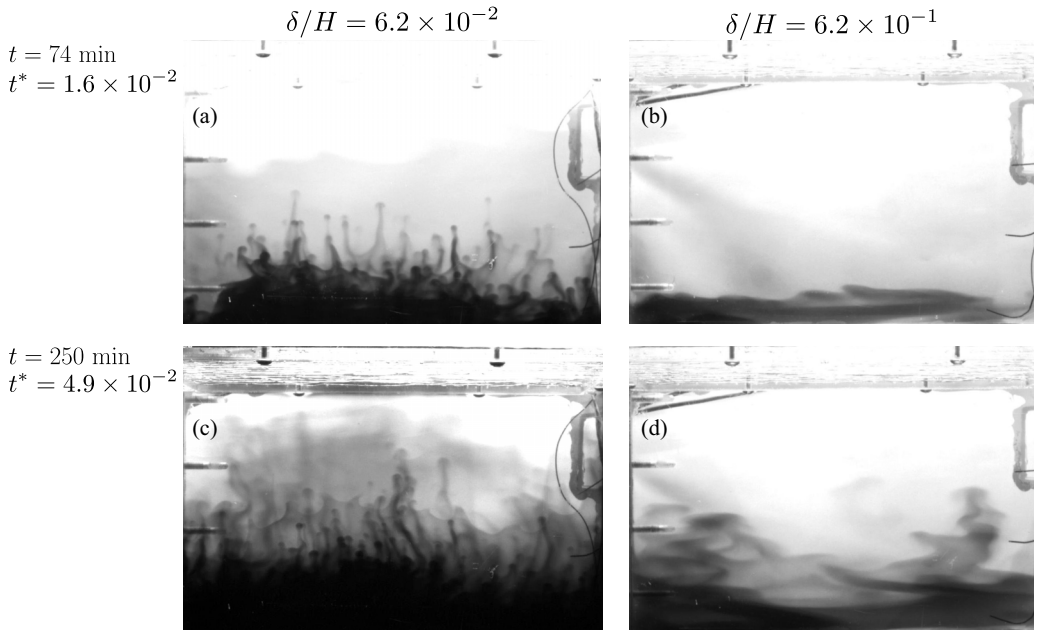

FIG. 2. Snapshots from two experiments taken at two different times. (a), (b) Pictures were taken 74 min after the start of the experiment and (c), (d) after 250 min. If we normalize the time by the thermal diffusive timescale across the box, the snapshots are taken at $t^* = 1.6 \times 10^{-2}$ and $t^* = 4.9 \times 10^{-2}$. The typical length of absorption, $\delta = 1/\varepsilon c_T$, is $\delta = 1.25$ cm for (a) and (c), and $\delta = 12.5$ cm for (b) and (d). We estimate the size of the plumes on (a) $\Lambda_1 \sim 1$ cm and on (d) $\Lambda_2 \sim 5$ cm. Full movies of the experiments are available in Supplemental Material [21].

concentrated in a small layer, while a low concentration results in a lower, more homogeneous heating across the blue layer. When varying c_T, we observe short wavelength instabilities developing at the top of the blue layer as shown in Figs. 2(a) and 2(c), while for low BTB concentration [Figs. 2(b) and 2(d)] we observe large wavelength instabilities. Quantitative estimates are challenging in this setup due to the fact that the camera visualization integrates the entire depth of the experimental domain, and the intense illumination causes image saturation. Nevertheless, we are able to estimate the typical wavelength Λ of the plumes in Fig. 2, which are in the nonlinear regime of the convective instability (this will be further discussed in Sec. V). For $c_T = 3.3 \times 10^{-5}$ mol/L [Fig. 2(a)] we estimate $\Lambda_1 \sim 1$ cm, and for $c_T = 3.3 \times 10^{-6}$ mol/L [Fig. 2(d)] we estimate $\Lambda_2 \sim 5$ cm. Finally, Fig. 2 demonstrates that the instabilities develop faster in the first case, consistent with the higher forcing in that experiment. The increase in both the instability wave number and growth rate with c_T is the most straightforward and consistently observable phenomena in our experimental setup, which we will now focus on explaining.

III. FULL NONLINEAR MODEL AND LINEARIZATION

A. Full nonlinear model

Defining the velocity $\vec{\mathbf{v}}$, pressure P, density ρ, reference density ρ_0, and kinematic viscosity ν, the Navier-Stokes equations in the Boussinesq approximation are

$$\frac{\partial \vec{\mathbf{v}}}{\partial t} + (\vec{\mathbf{v}} \cdot \vec{\nabla})\vec{\mathbf{v}} = -\frac{\vec{\nabla} P}{\rho_0} + \nu \Delta \vec{\mathbf{v}} - \frac{\rho}{\rho_0} g \vec{\mathbf{e}}_z; \quad \vec{\nabla} \cdot \vec{\mathbf{v}} = 0, \tag{1}$$

with $\vec{\mathbf{e}}_z$ the unit vector of the vertical coordinate z, oriented upward. The equation of state is

$$\rho = \rho_0[1 - \alpha(T - T_0)], \tag{2}$$

with T the temperature, T_0 the reference temperature, and α the thermal expansion coefficient. Defining Φ the irradiance going through the fluid, the energy gained by the absorption of light by a volume of fluid $\mathrm{d}\tau$ during a time $\mathrm{d}t$ is

$$\mathrm{d}E = \frac{\partial \Phi}{\partial z}\mathrm{d}\tau\,\mathrm{d}t. \tag{3}$$

Hence, defining the heat diffusion coefficient κ and the heat capacity at constant pressure c_p, the temperature equation is

$$\frac{\partial T}{\partial t} + \vec{\mathbf{v}} \cdot \vec{\nabla} T = \kappa \Delta T + \frac{1}{\rho_0 c_p}\frac{\partial \Phi}{\partial z}. \tag{4}$$

We suppose that light is only absorbed by the blue form of BTB and that absorption follows the Beer-Lambert law. We define c to be the concentration of the blue form of BTB. Then the Beer-Lambert equation is

$$\frac{\partial \Phi}{\partial z} = \varepsilon c \Phi, \tag{5}$$

and we can rewrite the temperature equation as

$$\frac{\partial T}{\partial t} + \vec{\mathbf{v}} \cdot \vec{\nabla} T = \kappa \Delta T + \frac{\varepsilon}{\rho_0 c_p} c\Phi. \tag{6}$$

We define $C = [\mathrm{HO}^-]$ to be the base concentration and $C_\mathrm{a} = [\mathrm{H}^+]$ to be the acid concentration. We assume that the reaction rate of the reaction $\mathrm{HO}^- + \mathrm{H}^+ \rightarrow \mathrm{H_2O}$ is proportional to the product of the concentration of each reactant, with rate constant k. Then, assuming that both species have the same diffusion coefficient D, the equations for C and C_a are

$$\frac{\partial C}{\partial t} + \vec{\mathbf{v}} \cdot \vec{\nabla} C = D\Delta C - k(C_\mathrm{a} C - c^{\circ 2} K_e), \tag{7}$$

$$\frac{\partial C_\mathrm{a}}{\partial t} + \vec{\mathbf{v}} \cdot \vec{\nabla} C_\mathrm{a} = D\Delta C_\mathrm{a} - k(C_\mathrm{a} C - c^{\circ 2} K_e), \tag{8}$$

with $K_e = 10^{-14}$ the ionic product of water and $c^\circ = 1\,\mathrm{mol/L}$ the standard concentration. Finally, we relate the blue concentration c to the base concentration C using the Henderson-Hasselbach equation, defining the acid dissociation constant of BTB, K_a, as

$$c = \frac{c_T C}{c^\circ K_e / K_a + C}. \tag{9}$$

The electrolysis produces a constant flux of base at the bottom of the tank and of acid at the top. Defining the Faraday constant F and n^-_{HO} the amount of substance of base, the electrolysis creates a flux of HO^- ions at the bottom, which is

$$\frac{\partial n^-_{\mathrm{HO}}}{\partial t} = \frac{I}{F}. \tag{10}$$

This flux is distributed over the area of the bottom surface S and diffuses upwards, leading to a bottom gradient of base concentration $\mathcal{F}$ in $\mathrm{mol\,L^{-1}\,m^{-1}}$,

$$\mathcal{F} = \frac{I}{10^3 FDS}, \tag{11}$$

and similarly for the top acid concentration gradient. The factor 10^3 is here to convert m^3 in L, the natural unit of concentrations. The complete set of boundary conditions at the top and bottom boundaries are

$$\vec{\mathbf{v}}(z=0) = \vec{\mathbf{v}}(z=H) = 0 \tag{12}$$

$$\Phi(z=H) = \Phi_0 \quad ; T(z=0) = 0; \quad T(z=H) = \Delta T \tag{13}$$

$$\left.\frac{\partial C}{\partial z}\right|_{z=0} = -\mathcal{F} \quad ; \quad \left.\frac{\partial C_\mathrm{a}}{\partial z}\right|_{z=0} = 0 \quad ; \quad \left.\frac{\partial C}{\partial z}\right|_{z=H} = 0 \quad ; \quad \left.\frac{\partial C_\mathrm{a}}{\partial z}\right|_{z=H} = \mathcal{F}. \tag{14}$$

The equations are solved using initial conditions, with pH_i the initial pH of the fluid:

$$\vec{\mathbf{v}} = 0 \quad ; \quad T = T_0 + \Delta T \frac{z}{H} \quad ; \quad C_\mathrm{a} = c^\circ 10^{-\mathrm{pH}_i} \quad ; \quad C = c^\circ 10^{\mathrm{pH}_i - 14}. \tag{15}$$

B. Linearization: Base state profiles and perturbation equations

To study the linear regime, we assume that the chemical reaction has no effect in the linear stage of the instability. Then it is not necessary to solve for the acid concentration field, and the reaction term in (7) disappears. We first determine the system base state by fixing the velocity to zero and compute the time evolution of base state temperature, $[HO^-]$ concentration, BTB blue form concentration, and irradiance profiles, respectively, T_b, C_b, c_b, and Φ_b. We will then perform a quasistatic stability analysis by looking for the growth of a perturbation about this slowly evolving base state.

We nondimensionalize the evolution equations using the heat diffusion timescale H^2/κ, the height of the tank H, and the BTB concentration c_T. Dimensionless variables are written with an *:

$$\begin{aligned} t = t^* \frac{H^2}{\kappa} \quad ; \quad z = z^* H \quad ; \quad \vec{\mathbf{v}} = \vec{\mathbf{v}}^* \frac{\kappa}{H} \quad ; \quad T - T_0 = T^* \Delta T \\ \Phi = \Phi^* \Phi_0 \quad ; \quad c = c^* c_\mathrm{T} \quad ; \quad C = C^* c_\mathrm{T}. \end{aligned} \tag{16}$$

With λ the thermal conductivity of the fluid, we introduce the following dimensionless numbers:

$$\mathrm{Le} = \frac{\kappa}{D} \quad ; \quad \beta = \frac{1}{\varepsilon c_\mathrm{T} H} = \frac{\delta}{H} \quad ; \quad Q = \frac{\Phi_0 \varepsilon c_\mathrm{T} H^2}{\lambda \Delta T} \quad ; \quad K^* = \frac{K_e c^\circ}{K_a c_\mathrm{T}}. \tag{17}$$

Changing the concentration of BTB has two effects: it affects the penetration depth (parametrized by β), and it affects the heating (parametrized by Q). With this nondimensionalization, the time evolution of the base profiles is given by

$$\frac{\partial T_\mathrm{b}^*}{\partial t^*} = \Delta T_\mathrm{b}^* + Q c_\mathrm{b}^* \Phi_\mathrm{b}^* \quad ; \quad \frac{\partial \Phi_\mathrm{b}^*}{\partial z^*} = \frac{1}{\beta} c_\mathrm{b}^* \Phi_\mathrm{b}^* \quad ; \quad \frac{\partial C_\mathrm{b}^*}{\partial t^*} = \frac{1}{\mathrm{Le}} \Delta C_\mathrm{b}^* \quad ; \quad c_\mathrm{b}^* = \frac{C_\mathrm{b}^*}{K^* + C_\mathrm{b}^*}, \tag{18}$$

with the initial conditions

$$T_b^*(t=0, z^*) = z^* \quad ; \quad C_b^*(t=0) = c^\circ / c_T \times 10^{\mathrm{pH}_i - 14}. \tag{19}$$

Examples of base profiles of temperature, HO^- and blue concentrations are given on Figs. 3 and 4. The temperature profile is initially linear and can be seen on Fig. 3. If the concentration of BTB is low, the heating is not sufficient to significantly change the temperature profile, which remains close to the initial one [Fig. 3(b)]. For a higher concentration and hence a higher heating, the profile will change significantly and an unstably stratified zone appears at late times [Fig. 3(a)]. The shape of base HO^- and blue concentration profiles are independent of the total BTB concentration. Initially the whole fluid is yellow, $C_\mathrm{b}(z, t=0) \simeq c_\mathrm{b}(z, t=0) \simeq 0$. Due to the bottom boundary condition,

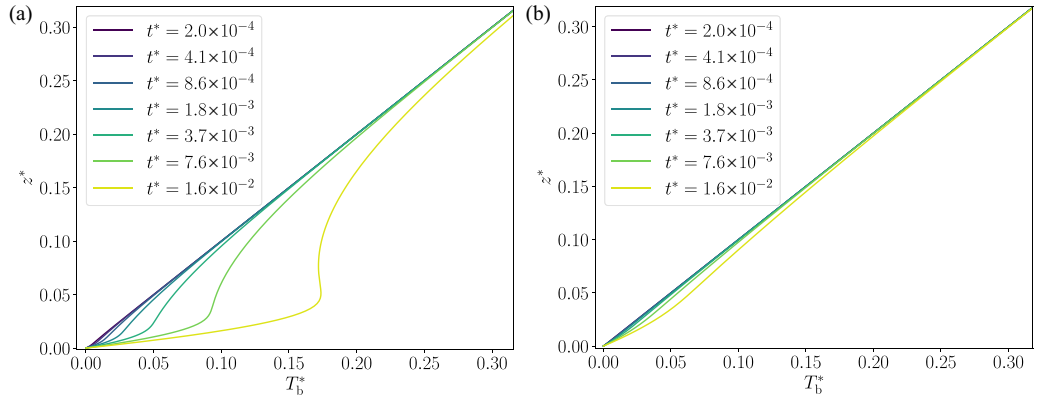

FIG. 3. Base temperature profiles, zoomed on the lower third of the domain, at different times, for simulations with parameters matching experiments shown in Fig. 2. In (a) $c_T = 3.3 \times 10^{-5}$ mol/L [corresponding to Figs. 2(a) and 2(c)], and in (b) $c_T = 3.3 \times 10^{-6}$ mol/L [corresponding to Figs. 2(b) and 2(d)].

a HO^- flux is produced at the bottom and the base diffuses upwards. As it diffuses, the fluid turns blue and a front of c_b^* propagates. The interface between this growing blue region and the ambient yellow fluid thickens by diffusion over time.

We now look for the perturbations above this slowly evolving base flow. We define the perturbations to the velocity, temperature, pressure, base concentration, BTB blue form concentration, and irradiance perturbations to be $\vec{\mathbf{v}}$, θ, P, C_p, c_p, and Φ_p, respectively. The linearized, dimensionless equations for the dimensionless perturbations then are

$$\frac{\partial \vec{\mathbf{v}}^*}{\partial t^*} = \mathrm{Pr}(-\nabla P^* + \Delta \vec{\mathbf{v}}^* + \mathrm{Ra}\theta \vec{\mathbf{e}}_z); \quad \vec{\nabla} \cdot \vec{\mathbf{v}}^* = 0, \tag{20}$$

$$\frac{\partial \Phi_p^*}{\partial z^*} = \frac{1}{\beta}(c_b^* \Phi_p^* + c_p^* \Phi_b^*), \tag{21}$$

$$\frac{\partial \theta}{\partial t^*} + w^* \frac{\partial T_b^*}{\partial z^*} = \Delta\theta + Q(c_b^* \Phi_p^* + c_p^* \Phi_b^*), \tag{22}$$

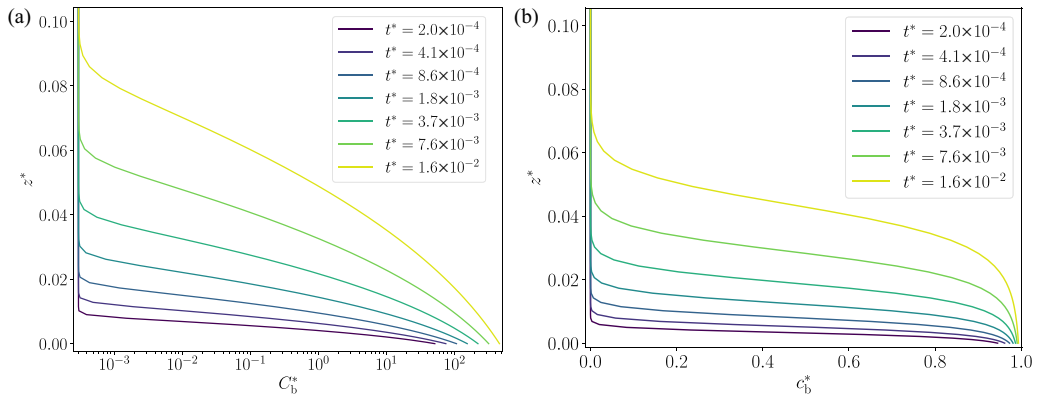

FIG. 4. Base [HO^-] (a) and blue concentration profiles (b), zoomed on the lower tenth of the domain, at different times. As c_T has no influence on c_b, these profiles are the same for the two simulatons.

$$\frac{\partial C_\mathrm{p}^*}{\partial t^*} + w^* \frac{\partial C_\mathrm{b}^*}{\partial z^*} = \frac{1}{\mathrm{Le}} \Delta C_\mathrm{p}^*, \tag{23}$$

$$c_\mathrm{p}^* = \frac{C_\mathrm{p}^* K^*}{(K^* + C_\mathrm{b}^*)^2}, \tag{24}$$

with w^* the dimensionless vertical velocity and the additional dimensionless numbers

$$\mathrm{Pr} = \frac{\nu}{\kappa} \quad ; \quad \mathrm{Ra} = \frac{\alpha g \Delta T H^3}{\kappa \nu}. \tag{25}$$

All the parameters match the experimental conditions, except K^*. Taking $K_e/K_a = 1 \times 10^{-7}$ would result in a transition from yellow to blue too sharp to be well resolved with our resolution. Instead we took $K_e/K_a = 1 \times 10^{-5}$. Typical values for our dimensionless parameters are the following:

$$\begin{aligned} &\mathrm{Pr} = 7 \quad ; \quad \mathrm{Ra} \sim 1.5 \times 10^9 \quad ; \quad \beta \sim 6.2 \times 10^{-2} - 6.2 \times 10^{-1} \quad ; \quad Q \sim 25.6 - 256 \\ &\mathrm{Le} = 100 \quad ; \quad K^* \sim 0.3 - 3. \end{aligned} \tag{26}$$

C. Instability mechanism

This set of base state and perturbation equations can be solved numerically to understand the physics of the instability, as will be done in the next section. Here, we give a qualitative explanation, keeping only the main terms in the perturbation equations as guided by the numerical simulations. In Eq. (20) we balance the vertical acceleration with the buoyancy term, which is the source of instability. In Eq. (22) the temperature growth is mainly due to the term containing the perturbation in blue concentration, neglecting heat diffusion and the background stratification. Finally in Eq. (23) we balance the increase of base concentration with the advection, since the diffusion of chemical species is very small ($\mathrm{Le} = 10^2$), and we keep Eq. (24) to relate c_p^* to C_p^*. This gives the following equations:

$$\frac{\partial w^*}{\partial t^*} \sim \mathrm{PrRa}\theta, \tag{27}$$

$$\frac{\partial \theta}{\partial t^*} \sim Q c_\mathrm{p}^* \Phi_\mathrm{b}^*, \tag{28}$$

$$\frac{\partial C_\mathrm{p}^*}{\partial t^*} \sim -w^* \frac{\partial C_\mathrm{b}^*}{\partial z^*}, \tag{29}$$

$$c_\mathrm{p}^* = \frac{C_\mathrm{p}^* K^*}{(K^* + C_\mathrm{b}^*)^2}. \tag{30}$$

Let us combine Eqs. (29) and (30) to directly estimate the growth of c_p^*:

$$\frac{\partial c_\mathrm{p}^*}{\partial t} \sim -w^* \frac{\partial C_\mathrm{b}^*}{\partial z^*} \frac{K^*}{(K^* + C_\mathrm{b}^*)^2} = -w^* \frac{\partial c_\mathrm{b}^*}{\partial z}. \tag{31}$$

On the right-hand side we identify the vertical derivative of the blue concentration base profile.

In Fig. 4(b) we can see that the interface between the blue region ($c_\mathrm{b}^* \sim 1$) and the yellow region ($c_\mathrm{b}^* \sim 0$) is sharp. Let us suppose that at some fixed point of this interface, the region where $\partial_z c_\mathrm{b}^* < 0$ and reaches an extremum, the fluid is hotter than its surroundings. Because it is hotter, the fluid at this place will experience a positive vertical velocity [Eq. (27)]. From Eq. (31), fluid initially lower

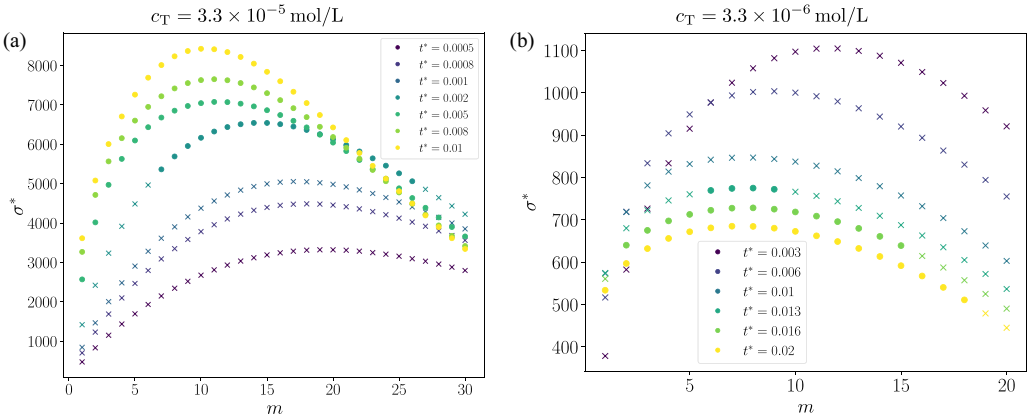

FIG. 5. Results from the linear stability analysis made using Dedalus [22]. Dots indicate that the quasistatic criterion is met, and hence that our analysis is justified (see Sec. IV A). (a) The experimental case with $c_T = 3.3 \times 10^{-5}$ mol/L shown in Fig. 2(a), and (b) to the experimental case with $c_T = 3.3 \times 10^{-6}$ mol/L shown in Fig. 2(b). The timescale on panel (a) is shorter than on panel (b): instabilities develop faster when the heating is greater.

than this point will be advected upward to the point, and hence the fluid at this point becomes bluer. Finally, from Eq. (28), as the fluid is bluer it heats more. The vertical velocity at this point then grows more, fluid become even bluer, becomes hotter, and so on. While this mechanism acts to destabilize the fluid, it is counterbalanced by the stabilizing effects of density stratification and diffusion of heat, momentum, and HO^-. This describes the base mechanism of our instability, which includes all the ingredients of the Rainy-Bénard convection [15]. It differs completely from the Rayleigh-Bénard instability; indeed, here the background density profile remains stably stratified, and the instability comes from a local runaway effect linked to the advection of the heat source (the blue fluid), which is further heated. In double diffusion also, the background density profile remains stably stratified: the destabilization then comes from the difference between the temperature diffusion and the concentration diffusion. In our case, the concentration does not appear in the equation of state but rather as a source term in the heat equation, and instability can happen even with $\mathrm{Le} = 1$.

IV. LINEAR STABILITY RESULTS

Quasistatic linear stability analysis is performed using the pseudospectral solver Dedalus [22]. We first solve for the time evolution of the one-dimensional base state (see Figs. 3 and 4 for examples of base profiles). Then, at each chosen time, the base flow is frozen, the perturbation problem is decomposed onto Fourier modes in the horizontal direction, and for each wave number m, we perform a one-dimensional eigenvalue solve to determine the fastest-growing eigenmode. Convergence tests were carried out to ensure the right choice of resolution; we use 256 Chebyshev polynomials in the vertical direction. The evolution of this fastest growth rate σ^* as a function of the mode number m and time t^*, corresponding to the two experimental cases, are shown in Fig. 5. Note that in all cases studied, the most unstable mode was always nonoscillatory, with no imaginary component in the growth rate.

A. Comparison with experiments

To compare numerical results and experiments, we need to define a criterion for estimating the most unstable mode in this transient process. This criterion should also be consistent with the quasistatic approach. The typical timescale of evolution of a perturbation mode is the inverse of

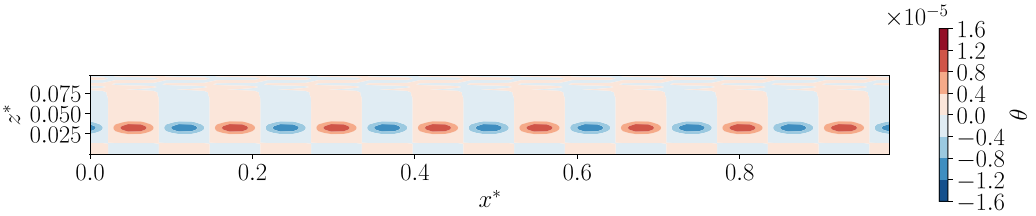

FIG. 6. Temperature perturbation for the most unstable mode, zoomed on the lower tenth of the domain, for $c_T = 3.3 \times 10^{-6}$ mol/L, corresponding to simulation results presented in Fig. 5(b).

its growth rate $1/\sigma^*(m)$. For the base profile, we take the time t^* as the characteristic timescale of evolution. We suppose that a perturbation is decoupled from the evolution of the base profile provided $\sigma^* t^* > 10$. The mode expected to grow in the corresponding experiment is then the one with the maximum $\sigma^*(m)$ computed at the smallest t^* for which at least one point validates the quasistatic criterion.

In Fig. 5 crosses indicate that the quasistatic criterion is not met whereas dots indicate that the criterion is met, hence our analysis is justified. The left panel of Fig. 5 corresponds to the experiment shown in Fig. 2(a), the right panel to Fig. 2(b). We thus expect a higher wave number and shorter destabilization time for the left panel than for the right one. In Fig. 5(a), the first curve satisfying the quasistatic criterion is for $t^* = 2 \times 10^{-3}$, where the most unstable mode number is $m = 14$. In Fig. 5(b), the first curve satisfying the criterion is for $t^* = 1.3 \times 10^{-2}$, where the most unstable mode number is $m = 8$. This mode is represented in Fig. 6.

These results are thus consistent with experimental observations. To check that they do not depend on the arbitrary quasistatic criterion $\sigma^* t^* > 10$, we plot in Fig. 7, for various threshold values of $\sigma^* t^*$, the onset time t^* and mode number m_{max} corresponding to the maximum growth rate for each simulation. For each chosen threshold value, dots, which correspond to Fig. 5(a), are always located more to the left and higher than triangles, which correspond to Fig. 5(b). This means that no matter the threshold of the quasistatic criterion, the instability occurs faster and at smaller scale in the first simulation than in the second, in agreement with the experimental observations.

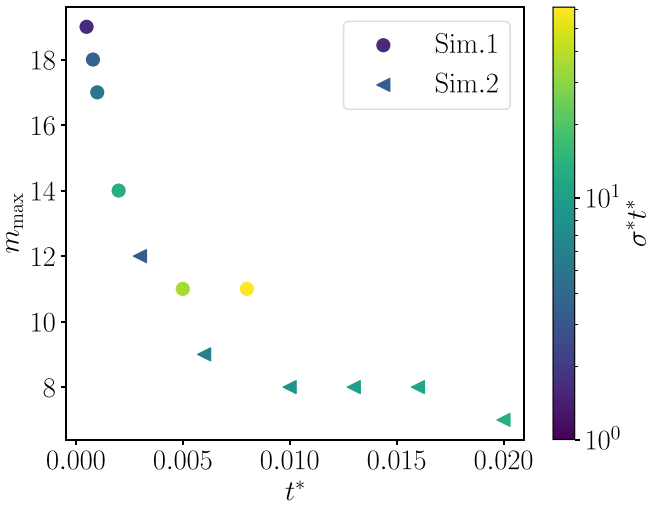

FIG. 7. Onset time of instability t^* and corresponding wave number m_{max} of the fastest-growing mode for various selected values of the instability criterion $\sigma^* t^*$ shown as a color scale. Dots correspond to the case shown in Fig. 5(a) and triangles to the case shown in Fig. 5(b).

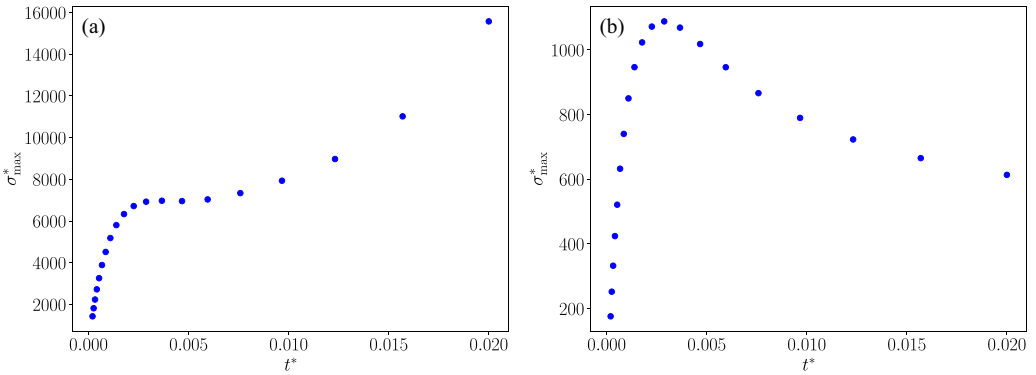

FIG. 8. Maximum growth rate vs time for each simulation, with $c_T = 3.3 \times 10^{-5}$ mol/L in (a) and $c_T = 3.3 \times 10^{-6}$ mol/L in (b).

Coming back to quantitative values, the instability's wavelengths estimated by linear stability analysis are

$$\Lambda_{1\text{num}} = H/14 \simeq 1.4\,\text{cm} \sim \Lambda_1; \quad \Lambda_{2\text{num}} = H/8 = 2.5\,\text{cm} < \Lambda_2. \tag{32}$$

Compared to experiments, linear stability analysis underestimates the typical flow scale in the second case. But one must recall that measurements in the experiments are not taken exactly at threshold: the transition from the length selected in the linear regime to the ones observed in the nonlinear regime will be the topic of Sec. V.

B. Evolution of the maximum growth rate with time

Examining Fig. 5, one might question why the maximum of σ^* increases with time in panel (a) while it decreases with time in panel (b). To investigate this evolution, we plot the maximum growth rate $\sigma^*_{\max}$ as a function of time for the two simulations in Fig. 8. Both curves initially exhibit a similar increasing trend but later diverge. The key distinction between the two simulations lies in the amount of heating provided and the associated penetration length, both depending on the BTB concentration c_T.

The primary effect of time evolution is on the base blue concentration profile, c^*_b [see Fig. 4(b)]. The depth of the interface zone between the blue and yellow regions, where the instability develops, is diffusive and thickens as $\sqrt{t^*/\text{Le}}$. Initially, the interface is very thin, which enhances diffusion efficiency, explaining why both curves grow at the start. But a thin interface also promotes instability growth: referring to the mechanism and Eq. (31), a thinner interface results in a steeper $-\partial_z c^*_b$ gradient, intensifying the instability. However, as diffusion smooths the blue concentration gradient, the growth rate decreases, as observed in Fig. 8(b). For the case shown in panel (a), we must also consider the evolution of the base temperature profile. Base temperature profiles at different times are plotted for each simulation in Fig. 3. In case (b), the heating is weaker, so the base temperature profile remains relatively stable over time. In contrast, in case (a), the heating is sufficient to significantly reduce the stratification in the interfacial region and even create an unstably stratified zone at around $t^* \sim 1.6 \times 10^{-2}$. This evolution of the background stratification enhances instability growth, explaining why $\sigma^*_{\max}$ continues to increase with time in the high-concentration case.

C. Influence of the penetration depth on the wavelength selection

The two experiments presented in Fig. 2 differ in their BTB concentration, which, as previously mentioned, affects both the magnitude of the heating and the corresponding penetration depth. An initial hypothesis for the selection of the observed wavelength as a function of BTB concentration could be that it is governed by the penetration depth $\delta = 1/(\varepsilon c_T)$ (expressed as β in the dimensionless formulation). However, revisiting our instability mechanism reveals that the critical dynamics

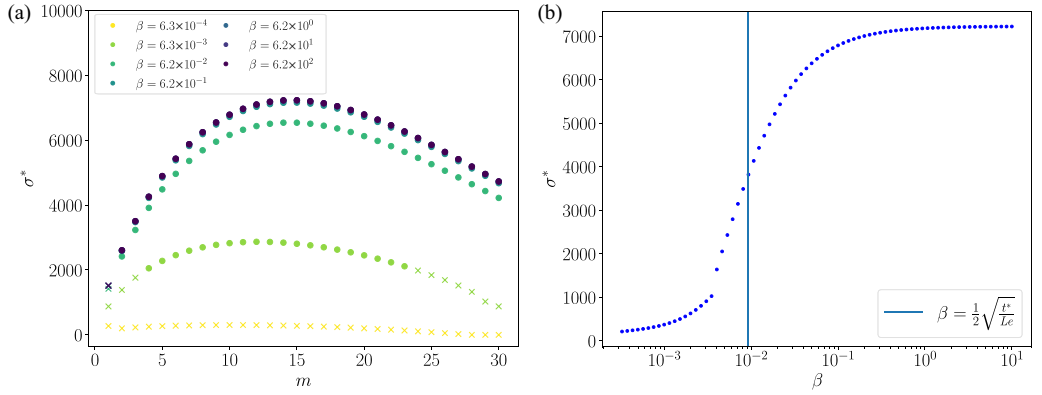

FIG. 9. (a) Maximum growth rate as a function of the mode number m for different values of β, all other parameters corresponding to the onset instability curve shown in Fig. 5(a). (b) Maximum growth rate as a function of the dimensionless penetration depth computed for $m = 14$. It is clear that for $\beta \gg 1/2\sqrt{\mathrm{Le}/t^*}$ (indicated by the vertical blue line), σ^* is largely independent of β. For small β, σ decreases until eventually the most unstable mode is another one.

occur at the interface, which has a dimensionless thickness $d \sim 1/2\sqrt{t^*/\mathrm{Le}}$. If the penetration depth significantly exceeds the thickness of the interface, it should have little to no influence on the instability. To test this hypothesis, we start from the onset instability curve shown in Fig. 5(a), where $\beta = 6.2 \times 10^{-2}$ (large c_T). Keeping all other parameters constant, we systematically varied β across a range from $\beta = 6.3 \times 10^{-4}$ to $\beta = 6.2 \times 10^{2}$ and calculated the growth rate evolution as a function of m for each case. The results are presented in Fig. 9 and confirm the expected trend. Since both experiments shown in Fig. 2 lie predominantly in the regime $\beta \gg 1/2\sqrt{t^*/\mathrm{Le}}$ ($6.2 \times 10^{-2} \leqslant \beta \leqslant 6.2 \times 10^{-1}$), it follows that the variation in penetration depth does not account for the difference between the two panels in Fig. 2. Instead, this difference must arise from the variation in the heating Q: greater heating results in higher growth rates, shorter time at which the quasistatic criterion is satisfied, and selection of a smaller wavelength.

V. PLUMES MERGING IN THE NONLINEAR REGIME

To address the quantitative mismatch between the wavelength estimates from the linear stability analysis and the experimental observations, direct numerical simulations (DNS) were performed using Dedalus [22]. These simulations solve the nonlinear set of equations described in Sec. III A, assuming an instantaneous chemical reaction. As a result, the reaction term in Eqs. (7) and (8) is set to zero, and chemical equilibrium is enforced in the main loop. The simulated equations are then

$$\frac{\mathrm{D}\vec{\mathbf{v}}^*}{\mathrm{D}t^*} = \mathrm{Pr}(-\vec{\nabla}P^* + \Delta\vec{\mathbf{v}}^* - \mathrm{Ra}T^*\vec{\mathbf{e}}_z); \quad \vec{\nabla}\cdot\vec{\mathbf{v}}^* = 0, \tag{33}$$

$$\frac{\mathrm{D}T^*}{\mathrm{D}t^*} = \Delta T + Qc^*\Phi^*, \tag{34}$$

$$\frac{\mathrm{D}C^*}{\mathrm{D}t^*} = \frac{1}{\mathrm{Le}}\Delta C^* \quad ; \quad \frac{\mathrm{D}C_\mathrm{a}^*}{\mathrm{D}t^*} = \frac{1}{\mathrm{Le}}\Delta C_\mathrm{a}^*, \tag{35}$$

$$\frac{\partial \ln(\Phi^*)}{\partial z} = \frac{c^*}{\beta}, \tag{36}$$

$$c^* = \frac{C^*}{K^* + C^*}, \tag{37}$$

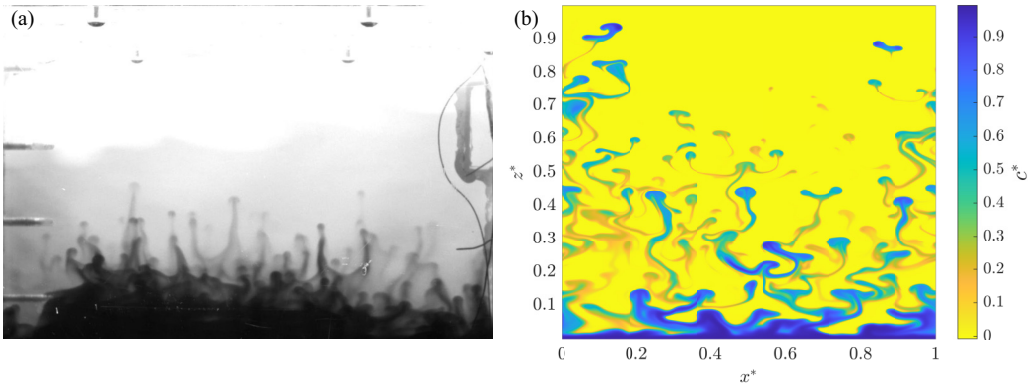

FIG. 10. Comparison between an experimental snapshot (a) and the corresponding DNS (b), taken at the same time. The dimensionless parameters of the simulations reproduce the experimental conditions apart from K^*. Here $Q = 256$ and $\beta = 6.2 \times 10^{-2}$.

with the boundary conditions Eqs. (12)–(14). Along with the initial conditions described in Eq. (15), random noise is added on the concentration and temperature fields to break the symmetry of the problem. Two simulations were conducted with parameters matching the experiments shown in Fig. 2. It is worth noting that, despite the relatively low Reynolds number (computed on the size of the domain with the maximum velocity, $\mathrm{Re} = v_{\max} H/\nu < 20$), these simulations were computationally challenging due to the sharp gradients in the concentration field of the blue form of BTB. Achieving sufficient resolution required a high number of coefficients; for instance, the simulation corresponding to Fig. 10(b) used 2048×2048 coefficients and Fig. 11(b) used 512×1024 coefficients (Fourier in x, Chebyshev in z). Snapshots of these simulations taken in the fully nonlinear regime and during the linear stage of the instability are plotted in Figs. 10–12.

The snapshot plotted in Figs. 10(b) and 11(b) are taken at a time corresponding to the experimental snapshots shown on the same figure. The DNS reproduces well the qualitative dynamics and size of plumes observed in the experiment, especially in the latter case. In Fig. 12 we can see the linear stage of the instability with, in each case, a mode of well defined wave number growing at the bottom of the domain. This is very similar to what has been shown in Fig. 6. We can compare the size of the mode in Fig. 12 with the size of the plumes in Figs. 10 and 11. For the (a) panels,

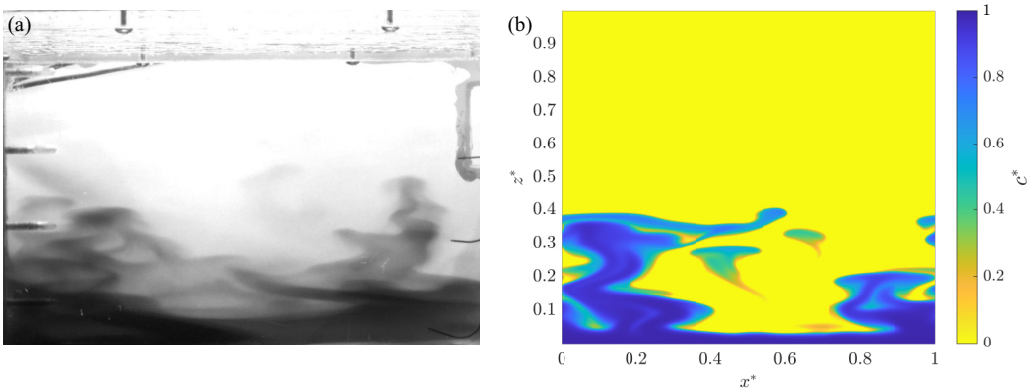

FIG. 11. Comparison between an experimental snapshot (a) and the corresponding DNS (b), taken at the same time. The dimensionless parameters of the simulations reproduce the experimental conditions apart from K^*. Here $Q = 25.6$ and $\beta = 6.2 \times 10^{-1}$.

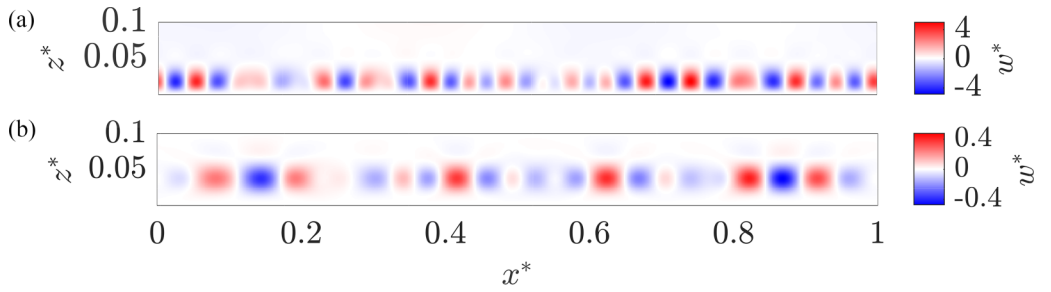

FIG. 12. Snapshots of the vertical velocity w^* from DNS with parameters matching the experiments shown in Fig. 2, zoomed on the lower tenth of the domain, (a) corresponds to Figs. 2(a) and 2(c) and (b) to Figs. 2(b) and 2(d). These snapshots are taken in the linear regime. Snapshot (a) was taken at $t^* = 3.2 \times 10^{-3}$, snapshot (b) was taken at $t^* = 1.7 \times 10^{-2}$.

the average size of plumes is not very different from the typical size of the linear mode, whereas for the (b) panels, the plumes have merged into one large structure larger than the features of the linear stage. This is consistent with the linear stability analysis predicting a smaller length scale for the flow in this case. Let us now analyze quantitatively the transition in length scale between the linear and the nonlinear regime.

To analyze this transition, the vertical velocity was first averaged along the vertical axis. At each time step, we computed the Fourier transform along the horizontal direction and normalized it by dividing by its maximum. Time was then rescaled by the inverse growth rate, determined from the initial evolution of the kinetic energy signal in each DNS. The results are presented in Fig. 13. For both panels of Fig. 13, initially the energy is distributed homogeneously over all wave numbers due to the random noise applied. This triggers internal gravity waves which decay, the ones of smaller wave number decaying slower because they are the less damped. That is what we observe in Fig. 13(a) for $0 < t_i < 15$ and in Fig. 13(b) for $0 < t_i < 8$, as well as traces in the background of Fig. 12. After that, the most linearly unstable mode grows exponentially in time.

In Fig. 13(a) the mode number selected during the linear regime is $m = 16$. As time progresses, plumes merge and the typical flow length scale increases. However, a wide dispersion of modes persist, including high mode number components. Conversely, in Fig. 13(b), where the linear mode number is $m = 10$, plume merging is significantly more efficient. For $t_i > 20$ most of the flow energy is concentrated in the single mode $m = 1$.

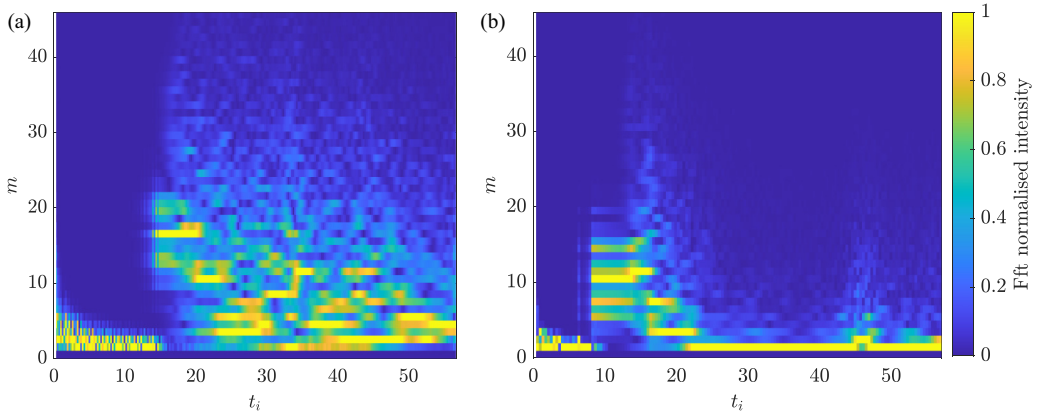

FIG. 13. Normalized horizontal Fourier transform of the vertical mean vertical velocity vs time. In each case, time is scaled by the inverse of the growth rate numerically defined by fitting the kinetic energy signal. In (a), parameters correspond to Fig. 2(a) and Fig. 5(a); in (b), parameters correspond to Fig. 2(b) and Fig. 5(b).

This behavior aligns with experimental observations and explains the mismatch between experimental measurements, which are taken in the nonlinear regime, and the predictions from the linear stability analysis. Furthermore, the mode numbers selected in the linear regime are consistent with linear predictions, which give $m = 14$ and $m = 8$ for the respective cases. This agreement validates the quasistatic approach and the criterion used in the previous section.

VI. CONCLUSION

In conclusion, we developed a setup replicating some aspects of moist convection. In the experiment a convective instability was observed, controlled by the concentration of the color indicator. To investigate this dependence, a complete model of the experiment was derived. A first-order force balance demonstrated that the observed instability arises from the advection of the heat source. The stabilizing effects are diffusion and ambient stratification. Linear stability analysis qualitatively reproduced the experimental observations at onset, while DNS illustrated the merging of instabilities in the nonlinear regime. In the low-concentration case, corresponding to a more homogeneous forcing, the plumes merge progressively, leading to the formation of a single dominant structure, reminiscent of the large cumulus clouds observed in the atmosphere.

However, in its current form, our experiment remains limited to low Reynolds numbers ($\mathrm{Re} < 20$), and accurate measurements present significant challenges. Furthermore, DNS of the model equations in two dimensions at these low Reynolds numbers already proves to be extremely computationally expensive. To approach regimes more relevant to atmospheric dynamics, we are currently developing an experiment with focused lighting. Additionally, we plan to perform local probe measurements instead of relying solely on nonintrusive visual techniques. In summary, our system is intellectually stimulating and visually engaging. However, proving its utility for advancing our understanding of moist convection requires further development and exploration.

ACKNOWLEDGMENTS

The initial ideas for this study were developed during discussions between D.L. and M.L.B. while they were both visiting the Geophysical Fluid Dynamics Program at WHOI in 2020. We gratefully acknowledge the program for providing such a stimulating scientific environment. D.L. is supported in part by NASA OSTFL Grant No. 80NSSC22K1738, Sloan Foundation Grant No. FG-2024-21548, and Simons Foundation Grant No. SFI-MPS-T-MPS-00007353. M.L.B. is supported in part by Simons Foundation Grant No. SFI-MPS-T-MPS-00007353.

DATA AVAILABILITY

The data that support the findings of this article are openly available [23].

APPENDIX: COMPARISON WITH THE "RAINY-BÉNARD" MODEL

The full set of equations of the Rainy-Bénard model [15] is as follows:

$$\frac{\mathrm{D}\vec{\mathbf{v}}}{\mathrm{D}t} = -\vec{\nabla}\varphi + \nu\Delta\vec{\mathbf{v}} + b\vec{\mathbf{e}}_z\,; \quad \vec{\nabla}\cdot\vec{\mathbf{v}} = 0, \tag{A1}$$

$$\frac{\mathrm{D}b}{\mathrm{D}t} = \gamma\frac{q-q_s}{\tau}\mathcal{H}(q-q_s) + \kappa\Delta b, \tag{A2}$$

$$\frac{\mathrm{D}q}{\mathrm{D}t} = -\frac{q-q_s}{\tau}\mathcal{H}(q-q_s) + \kappa_q\Delta q, \tag{A3}$$

$$T = \frac{T_0 g}{b} - \frac{gz}{c_p}, \tag{A4}$$

$$q_s = q_0 \mathrm{e}^{\chi T}, \tag{A5}$$

where $\varphi = P/\rho_0$ (P including the hydrostatic balance), b is buoyancy, q is the specific humidity, q_s saturation humidity, κ_q the diffusion coefficient of water vapor, τ the "fast" timescale of condensation, γ, q_0, T_0, and χ are constants, $\mathcal{H}$ is the Heaviside function, c_p the specific heat, and g gravity.

The full set of equations describing our experiment is

$$\frac{\mathrm{D}\vec{\mathbf{v}}}{\mathrm{D}t} = -\vec{\nabla}\varphi + \nu\Delta\vec{\mathbf{v}} + \alpha(T - T_0)g\vec{\mathbf{e}}_z; \quad \vec{\nabla}\cdot\vec{\mathbf{v}} = 0, \tag{A6}$$

$$\frac{\mathrm{D}T}{\mathrm{D}t} = \frac{\varepsilon c_\mathrm{T}}{\rho_0 c_p}\frac{C}{c^\circ K_e/K_a + C}\Phi + \kappa\Delta T, \tag{A7}$$

$$\frac{\mathrm{D}C}{\mathrm{D}t} = -k(C_\mathrm{a}C - c^{\circ 2}K_e) + D\Delta C, \tag{A8}$$

$$\frac{\mathrm{D}C_\mathrm{a}}{\mathrm{D}t} = -k(C_\mathrm{a}C - c^{\circ 2}K_e) + D\Delta C_\mathrm{a}, \tag{A9}$$

$$\frac{\partial\Phi}{\partial z} = \frac{\varepsilon c_T C}{c^\circ K_e/K_a + C}\Phi. \tag{A10}$$

In our model, the concentration C is the analog of q. The two buoyancy equations, Eqs. (A2) and (A7), have internal heating terms which include the Heaviside function in Rainy-Bénard and a Michaelis-Menten–type function in ours, both exhibiting a sharp threshold.

Both models include a "fast" return to equilibrium, as we can see in Eqs. (A3) and (A8). The humidity q returns to its saturation value on the timescale τ, which is very small, and the concentration C returns to chemical equilibrium on the timescale $1/k$, which is also very small.

In the Rainy-Bénard model, the humidity decreases when the water condensates; in our model the base concentration decreases because it reacts with acid. This nonperfect analogy "breaks" the symmetry present in the Rainy-Bénard model, where one can define $m = b + \gamma q$, which then verifies an advection-diffusion equation. In our case such a quantity does not exist.

Our model does not include the effect of compressibility on temperature [Eq. (A4)], as well as the effect of temperature on the threshold [Eq. (A5)]. Finally, the Beer-Lambert equation [Eq. (A10)], which makes the heating nonhomogeneous in the blue layer, is not present in the Rainy-Bénard model.

[1] F. Chillà and J. Schumacher, New perspectives in turbulent Rayleigh-Bénard convection, Eur. Phys. J. E **35**, 58 (2012).

[2] T. Radko, *Double-Diffusive Convection* (Cambridge University Press, Cambridge, England, 2013).

[3] E. Kunze, A review of oceanic salt-fingering theory, Prog. Oceanogr. Double-Diffusion in Oceanography, **56**, 399 (2003).

[4] A. Oschlies, H. Dietze, and P. Kähler, Salt-finger driven enhancement of upper ocean nutrient supply, Geophys. Res. Lett. **30**, 2204 (2003).

[5] S. Kato, Overstable convection in a medium stratified in mean molecular weight, Publ. Astron. Soc. Jpn. **18**, 374 (1966).

[6] A. Toramaru and M. Matsumoto, Numerical experiment of cyclic layering in a solidified binary eutectic melt, J. Geophys. Res. **117**, B02209 (2012).

[7] S. Schoofs, F. J. Spera, and U. Hansen, Chaotic thermohaline convection in low-porosity hydrothermal systems, Earth Planet. Sci. Lett. **174**, 213 (1999).

[8] S. Lepot, S. Aumaître, and B. Gallet, Radiative heating achieves the ultimate regime of thermal convection, Proc. Natl. Acad. Sci. USA **115**, 8937 (2018).

[9] M. H. P. Ambaum, *Thermal Physics of the Atmosphere* (Elsevier, New York, 2020).

[10] P. Warneck, Jost Heintzenberg and Robert J. Charlson (eds): Clouds in the perturbed climate system; Their relationship to energy balance, atmospheric dynamics, and precipitation, J. Atmos. Chem. **62**, 87 (2009).
[11] J. P. Mellado, Cloud-top entrainment in stratocumulus clouds, Annu. Rev. Fluid Mech. **49**, 145 (2017).
[12] G. L. Mellor and T. Yamada, A hierarchy of turbulence closure models for planetary boundary layers, J. Atmos. Sci. **31**, 1791 (1974).
[13] O. Pauluis and J. Schumacher, Self-aggregation of clouds in conditionally unstable moist convection, Proc. Natl. Acad. Sci. USA **108**, 12623 (2011).
[14] S. Grossmann and D. Lohse, Scaling in thermal convection: A unifying theory, J. Fluid Mech. **407**, 27 (2000).
[15] G. K. Vallis, D. J. Parker, and S. M. Tobias, A simple system for moist convection: The Rainy–Bénard model, J. Fluid Mech. **862**, 162 (2019).
[16] R. Narasimha, S. S. Diwan, S. Duvvuri, K. R. Sreenivas, and G. S. Bhat, Laboratory simulations show diabatic heating drives cumulus-cloud evolution and entrainment, Proc. Natl. Acad. Sci. **108**, 16164 (2011).
[17] H. Fu, C. Cenedese, A. Lefauve, and G. K. Vallis, A laboratory analogy for mixing by shallow cumulus convection, J. Fluid Mech. **1011**, A35 (2025).
[18] B. J. Sayler and R. E. Breidenthal, Laboratory simulations of radiatively induced entrainment in stratiform clouds, J. Geophys. Res.: Atmos. **103**, 8827 (1998).
[19] R. Krishnamurti, Convection induced by selective absorption of radiation: A laboratory model of conditional instability, Dyn. Atmos. Oceans **27**, 367 (1998).
[20] C. Almarcha, P. M. J. Trevelyan, L. A. Riolfo, A. Zalts, C. El Hasi, A. D'Onofrio, and A. De Wit, Active role of a color indicator in buoyancy-driven instabilities of chemical fronts, J. Phys. Chem. Lett. **1**, 752 (2010).
[21] See Supplemental Material at http://link.aps.org/supplemental/10.1103/PhysRevFluids.10.053505 for the full movies of experiments.
[22] K. J. Burns, G. M. Vasil, J. S. Oishi, D. Lecoanet, and B. P. Brown, Dedalus: A flexible framework for numerical simulations with spectral methods, Phys. Rev. Res. **2**, 023068 (2020).
[23] V. Dorel, 2025, https://amubox.univ-amu.fr/s/MfYKKwwMQpaKsef.